

## INVESTIGATION ON THE BEHAVIOUR OF HIGH REYNOLDS ROUND IMPINGING ZERO-NET-MASS-FLUX JETS

**Carlo Salvatore Greco**  
 Department of Industrial Engineering  
 University of Naples Federico II  
 Piazzale Tecchio, 80 - Naples Italy  
 carlosalvatore.greco@unina.it

**Gennaro Cardone**  
 Department of Industrial Engineering  
 University of Naples Federico II  
 Piazzale Tecchio, 80 - Naples Italy  
 gennaro.cardone@unina.it

**Julio Soria**  
 Department of Mechanical and Aerospace Engineering  
 Laboratory for Turbulence Research in Aerospace and Combustion - Monash University  
 Clayton campus - Melbourne Australia  
 Department of Aeronautical Engineering  
 King Abdulaziz University, Jeddah Kingdom of Saudi Arabia  
 julio.soria@monash.edu

### INTRODUCTION

A zero-net-mass-flux (ZNMF) jet is a fluid stream with non-zero mean streamwise momentum formed oscillatory flow through an orifice (Cater and Soria, 2002). The ZNMF jet is generated within the fluid in which the generator is embedded without the net injection of additional fluid. Typically ZNMF jets can be generated using a periodic oscillatory membranes as loudspeakers (Greco et al., 2013) and piezoelectric diaphragms (Smith and Glezer, 1998) or using a mechanical piston-cylinder arrangement (Cater and Soria, 2002). Due to this periodic movement the fluid is entrained into the cavity and consequently expelled through the orifice completing the cycle. Under certain operating condition (Holman et al., 2005), a vortex ring can form near the orifice and convects away. The dimensionless groups, that characterize ZNMF jets, are the Reynolds number ( $Re = U_0 D_0 / \nu$ ) and the Strouhal number ( $f D_0 / U_0 = D_0 / L_0$ ), where  $U_0$  is a characteristic velocity scale,  $D_0$  is the orifice diameter,  $\nu$  is the water kinematic viscosity,  $f$  is the actuation frequency and  $L_0$  is the stroke length (defined as  $U_0 / f$ ) that is associated to the quantity of fluid pulled in the ambient during the expulsion cycle. Cater and Soria (2002) define this characteristic velocity as :

$$U_0 = \sqrt{\frac{4}{\pi D_0^2 \tau} \int_0^\tau \int_0^{\frac{D_0}{2}} 2\pi r u_0(r,t) u_0(r,t) dr dt} \quad (1)$$

where  $\tau$  is the actuation period and  $u_0$  is the velocity at the exit plane of the orifice.

The literature on ZNMF jets is very wide and includes several fields of applications such as: flow control, heat transfer, enhancement of mixing between fluid currents and generation of microthrust for propulsion. Focusing our attention on the heat transfer field, it is possible to note that a wide literature is present describing and evaluating the heat transfer capabilities of ZNMF jets (Greco et al., 2014; and

Valiourge et al., 2009). Instead not so wide is the literature on the characterization of the impinging flow field of such jets. Pavlova and Amitay (2006) experimentally studied the influence of Reynolds number ( $140 \leq Re \leq 740$ ), orifice-to-plate distance ( $1.9 D_0 \leq H \leq 38.1 D_0$ ) and formation frequency (equal to 420 and 1200 Hz) on the heat transfer rate. At low operating frequency, the vortex ring impinges individually causing the heat transfer enhancement while, at high operating frequency, the vortex ring merge and break into smaller secondary structures generating the heat transfer increase. Valiourge et al. (2009) studied ZNMF jets impinging at nozzle-to-plate distance equal to  $2 D_0$  and for various stroke lengths ( $1 < L_0 / D_0 < 22$ ) and Reynolds number (between 1000 and 4300). The heat transfer rate (that obviously increases with increasing Reynolds number) was found to increase linearly with  $L_0 / H$  up to  $L_0 / H = 2.5$ , then being constant. They also found a correlation between the impinging vortex dynamics and the local heat transfer profile. Indeed the extent of the central region of high heat transfer corresponds to the vortex impingement location, while, the region outside the central one is determined by the distance travelled by the coherent vortex. The effect of the stroke length on the flow morphology of ZNMF jets was studied by McGuinn et al. (2013) with high speed PIV and hot wire anemometry. They found that ZNMF jets without impingement are characterized by a monotonous increase in vortex strength up to  $L_0 / D_0 = 4$ . For  $L_0 / D_0$  higher than 4 and up to 8 the flow field is characterized by additional fluid ejected after the formation of the vortex ring and forming a trailing jet following and widening the vortex ring. A maximum ejection velocity occurs in the trailing jet and destabilizes the vortex ring promoting mixing for  $L_0 / D_0$  between 8 and 16. For higher  $L_0 / D_0$  the most relevant flow feature is represented by the trailing jet: the ejected fluid, remaining once the primary vortex is fully formed and propagated, overtakes the vortex ring resulting in a highly turbulent jet. The aim of this paper is to provide

a detailed insight on the impinging ZNMF jet flow field features at high Reynolds number (35000) for several values of Strouhal number (0.044, 0.022 and 0.011). For every case, three different dimensionless values of the orifice-to-plate distance ( $H/D_0$ ) are investigated: 2, 4 and 6.

## EXPERIMENTAL SETUP

Experiments are undertaken in a rig depicted in Figure 1. In each experiment, ZNMF jets are generated by using a reciprocating piston within a cylinder which discharges water from a circular cylinder with inner diameter  $D_p = 50$  mm through an orifice plate of a given diameter  $D_0 = 10$  mm and thickness of 2 mm. The distance ( $H$ ) between the orifice plate and the impinging plate is adjusted by using a linear bearing located on the top. The piston is connected to an AC motor through a flexible coupling and an eccentric plate. Setting up the half piston stroke  $l_p$  (2, 4 and 8 mm) and the piston frequency (or actuation frequency  $f$  equal to 16, 8 and 4 Hz), the desired ZNMF jet is obtained. The water is seeded with hollow glass spheres (Potter spherical, with a density of  $1100 \text{ kg/m}^3$ ) with a nominal diameter of  $11 \mu\text{m}$  having a relaxation time of  $7.39 \mu\text{s}$ . A pump is used to homogenize the water and particles inside the tank to reach a high uniformity. The particles are illuminated by a Quantronix Nd: YLF twin cavity laser system capable of supplying 30 mJ/pulse at a wavelength of 527 nm. The thickness of the laser sheet is adjusted to 1 mm and the laser sheet is aligned vertically including the jet axis. The time difference between two laser pulses is  $40 \mu\text{s}$ . The scattered light from the particles is recorded on a PCO-DIMAX high speed cameras with CMOS array size  $2016 \times 2016 \text{ pixel}^2$ . The camera is mounted with 100 mm Zeiss lens and f-stop number is set up to 2. The camera acquires at its maximum acquisition rate of 624 Hz (in a double frame configuration) and the field of view is approximately  $6.3 D_0 \times 6.3 D_0$ . The resulting resolution for the digital images is  $31.33 \mu\text{m/pixel}$  in the illumination plane. Both camera and laser are synchronized by a delay generator (DG645) which starts generating signals when the hall sensor detects the lowest piston position during its oscillation. The switch Trigger/Camera allows to start acquiring images when the phenomenon is steady. Vector fields were obtained processing images with a multigrid cross-correlation digital particle velocimetry (MCCD-PIV) analysis which is described in Soria (1996 and 1998). The accuracy and uncertainty associated with multigrid cross-correlation PIV measurements are investigated and discussed in Soria (1996 and 1998). For the first pass the size of the interrogation window was 64 pixel, while for the second pass 32 pixel windows were used. The sample spacing between the centres of the interrogation windows was 16 pixels (50% of overlap).

## TRIPLE DECOMPOSITION ANALYSIS

The obtained data are analysed by using a triple decomposition (Hussain and Reynolds, 1970):  $u_i(\underline{x}, t) = U_i(\underline{x}) + \tilde{u}_i(\underline{x}, t) + u'_i(\underline{x}, t)$ , where  $u_1 = u$ ,  $u_2 = v$ ,  $u_3 = w$  and  $x = (x, y, z)$ .  $U_i$  is the time-average,  $\tilde{u}_i$  is the phase-correlated organised contribution to the velocity and  $u'_i$  is the turbulent velocity fluctuation. The time-average velocity is defined as:  $U_i(\underline{x}) = \lim_{\tau \rightarrow \infty} \frac{1}{\tau} \int_0^\tau u_i(\underline{x}, t) dt$ ; while the phase-average velocity is:  $\langle u_i(\underline{x}, t) \rangle = \lim_{N \rightarrow \infty} \frac{1}{N} \sum_{n=0}^{N-1} u_i(\underline{x}, t + n\tau)$ , where  $N$  is the number of flow fields of the same phase,  $\tau$  is the period of the or-

ganised contribution, whose reciprocal coincides with the actuation frequency  $f$ . Hence the phase-average velocity is the average in any spatial point for a fixed phase  $\varphi$  in the ZNMF jet generation cycle. The phase-correlated organised contribution to the velocity is then defined as:

$$\tilde{u}_i(\underline{x}, t) = \langle u_i(\underline{x}, t) \rangle - U_i(\underline{x}) \quad (2)$$

while the turbulent velocity fluctuation is:

$$u'_i(\underline{x}, t) = u_i(\underline{x}, t) - \langle u_i(\underline{x}, t) \rangle \quad (3)$$

## RESULTS AND DISCUSSION

In Figures 2-9 the phase-average velocity components maps at  $H/D_0$  equal to 2 and 6 for  $Sr$  equal to 0.011 and 0.044 are shown. The same phases are reported for the two Strouhal number cases. Only 10 phases (for the  $H/D_0$  equal to 2) and 9 phases (for the  $H/D_0$  equal to 6), with a step of  $18.46^\circ$ , are chosen in order to represent the ejection cycle. In Figure 2 the axial and radial velocity maps at  $H/D_0$  equal to 2, for  $Sr$  equal to 0.011, are depicted. At  $\varphi = 0^\circ$  the ejection phase starts while at  $\varphi = 18.46^\circ$  the vortex ring is already completely formed and the following trailing jet is easily detectable on its behind. Then the ZNMF jet impinges and, at  $\varphi = 36.92^\circ$ , it is sweeping the impinging plate. At this phase, it is possible to see that the axial velocity profile is not bell-shaped near the impinging plate. Indeed a minimum of the local axial velocity is observable on the jet axis ( $x/D_0$  equal to 0) near the stagnation zone. Such a behaviour is due to the adverse pressure gradient caused by the impinging plate presence. The radial velocity component shows two maxima: the first one where the jet rotation is detectable (near the impinging plate at  $x/D_0$  equal to about 0.5) and the second one that is placed between the sweeping vortex ring and the plate. At  $\varphi = 55.38^\circ$  the values of the region of high axial velocity are increased and the vortex ring is moving out of the measurement zone. For  $55.38^\circ < \varphi < 92.30^\circ$  the behaviour of the ZNMF jet does not show any substantial differences and resembles the continuous jet one. For  $\varphi \geq 92.30^\circ$  the axial and radial velocity decrease. In Figure 3 the mean squared axial and radial turbulent velocity maps at  $H/D_0$  equal to 2, for  $Sr$  equal to 0.011, are shown. The ZNMF jet starts being issued at  $\varphi = 0^\circ$  and at  $\varphi = 18.46^\circ$  it is characterized by a peak of axial turbulent near the vortex core. Also a value different from zero is observable along the shear layer. The radial component attains its maximum in the vortex ring core as well. At  $\varphi = 36.92^\circ$  high values of radial and axial turbulence are present along the shear layer but their maxima are still located in the vortex ring core. Furthermore, regarding to the radial component, another two maxima are visible: the first one is located where the complete rotation of the jet occurs and the second one is between the vortex ring and the impinging plate. Such a second peak could be caused by a counter-rotating vortex (see Hadžiabdić and Hanjalić, 2008) generated by the sweeping vortex ring. Moreover also a small no-zero turbulent region is present on the nozzle exit centre. At  $\varphi = 55.38^\circ$  the axial turbulent velocity component still shows high values along the shear layer and in the vortex ring core while the radial one has its maximum in the vortex ring core and also in the region near the plate which spans from the impinging shear layer to the vortex ring ( $x/D_0$  ranging between 0.7 and 2). Moreover the radial

component shows high values along the shear layer and low values in the region near the jet axis (which starts from the nozzle exit). Considering the phases ranging from  $73.84^\circ$  to  $92.30^\circ$  any sensitive differences are observed, while for  $\varphi > 92.30^\circ$  the turbulent values decrease. It is possible to point out that during this ejection phase no merging of the shear layer is detectable. This leads to have a zone, along the jet axis, featured by zero axial turbulence level and low radial one. Such a region, already shown for free ZNMF jets in Greco et al. (2013), resembles the potential core region present in continuous jets (Abramovich, 1963). In Figure 4 the axial and radial velocity components are depicted for a  $Sr$  equal to 0.044 at  $H/D_0$  equal to 2. As for the previous case, at  $\varphi = 0^\circ$  the generation of the ZNMF jet starts. At  $\varphi = 18.46^\circ$  the vortex ring is forming and starts its convection (see also  $\varphi = 36.92^\circ$ ) until it reaches the impinging plate ( $\varphi = 73.84^\circ$ ). At this phase (i.e.  $\varphi = 73.84^\circ$ ) the “sweeping phase” starts and two regions of high radial velocity can be detected easily at  $\varphi = 92.30^\circ$ . These two regions are, as usual, located near the deflection zone of the impinging ZNMF jet (at  $x/D_0$  equal to 0.5) and between the sweeping vortex ring and the impinging plate. The axial velocity component near the plate exhibits the usual profile with a local minimum on the jet axis ( $x/D_0$  equal to 0). At  $\varphi \geq 92.30^\circ$  the axial velocity decrease while the vortex ring is still in the measurement zone. Indeed the displacement of the vortex ring scales with the stroke length (Shuster and Smith, 2007). At  $\varphi = 110.76^\circ$  the first peak of radial velocity at  $x/D_0$  equal to about 0.5 is decreasing because the jet axial velocity is reducing while the second peak is still clearly visible and high. As matter of fact at  $\varphi = 129.22^\circ$  the second radial peak is much higher than the first one which is almost disappeared. Only for  $\varphi \geq 166.14^\circ$  the vortex ring is moved completely out of the region of measurement. Such a behaviour is strictly related to the Strouhal number. At high Strouhal number the trailing jet, following the vortex ring, decreases. Such a phenomenon leads to have a flow field much more influenced by the vortex ring presence. In Figure 5 the mean squared axial and radial turbulent velocity maps at  $H/D_0$  equal to 2, for  $Sr$  equal to 0.044, are shown. From  $\varphi = 0^\circ$  to  $\varphi = 73.84^\circ$  the ZNMF jet is formed and convects until the impinging plate. During these phases, the high values of radial and axial turbulent velocity are mainly located in the vortex ring core and along the shear layer. Even for this Strouhal number case, it is possible to highlight that a no zero value of radial turbulence is observable on the nozzle exit and it extends until the impinging plate. At  $\varphi = 92.30^\circ$  the vortex ring is sweeping the plate and the maximum, for the axial turbulent component, is detected in the vortex ring core. A similar behaviour characterizes also the radial turbulent component that also shows high values near the plate (in the region connecting the impinging shear layer and the vortex core) and in the region near the plate (ahead of the vortex ring) where the counter rotating vortex should be arisen by the passage of the vortex ring. For both components, high values are observed along the shear layer. At  $\varphi = 110.76^\circ$  both turbulent components still have the maximum in the vortex ring core and the radial one shows a greater second peak (the one ahead of the vortex ring). Moreover the radial turbulent component shows a region of high values, with a greater extension, near the impinging plate. Nevertheless, the values along the shear layer are slightly decreased while the maxima near the vortex ring core are still visible. For  $\varphi \geq 129.22^\circ$  the values near the plate and along the shear

layer decrease differently from the value in the vortex ring core. Even for this configuration no merging of the shear layer can be observed and a zone, featured by zero axial turbulence and low radial one, is observable near the jet axis. Furthermore it has to be point out that the turbulent values attained near the vortex ring core are definitely higher than the case at  $Sr$  equal to 0.011 but similar to those at  $Sr$  equal to 0.022. In Figure 6 the axial and radial velocity distributions, for  $Sr$  equal to 0.011 at  $H/D_0$  equal to 6, are shown. The ZNMF jet is issued (at  $\varphi = 0^\circ$ ) then convects (at  $\varphi$  equal to  $18.46^\circ$  and  $36.92^\circ$ ) until it reaches the impinging plate. It is possible to see that, at  $\varphi = 36.92^\circ$ , the maximum of the axial velocity is not in the centre of the vortex ring but is located on the jet axis (in the following trailing jet). This agrees to what shown by McGuinn et al. (2013) who found that the maximum velocity of a ZNMF jet is not detected in the vortex ring centre but in the trailing jet for high  $L_0/D$  values (or low  $Sr$  values). At  $\varphi = 55.38^\circ$  and  $\varphi = 73.84^\circ$  the ZNMF jet has already spread over the plate and is sweeping the plate itself. During these phases, the radial velocity shows a maximum between the plate and the vortex ring which is higher than the one located in the rotation region of the impinging ZNMF jet. This is also related to the axial velocity profile which approaches the impinging plate. Indeed in this case ( $H/D_0$  equal to 6) the profile is bell-shaped not causing a great peak of radial velocity as occurs for the shortest case (Figure 2). At  $\varphi$  equal to  $73.84^\circ$ , the vortex ring is almost out of the measurement zone and the flow field resembles the impinging continuous one. Furthermore a mild peak of high radial velocity is still located near the plate where the impinging ZNMF jet rotates. For  $\varphi \geq 92.30^\circ$  the axial and radial velocity values decrease. In Figure 7 the mean squared axial and radial turbulent velocity component, for  $Sr$  equal to 0.011 at  $H/D_0$  equal to 6, are depicted. At  $\varphi = 18.46^\circ$  the first values, different from zero, are observed. As usual, the high turbulent values are located near the vortex core and along the all shear layer (axial turbulence) or a part of it (radial turbulence). At  $\varphi = 36.92^\circ$  the values are increasing near the vortex ring core while the shear layer is wider and more extended. It has to be highlighted that the axial turbulent velocity component shows high values also on the front boundary of the vortex ring but not in its centre (located on the jet axis), differently from the radial component. At  $\varphi = 55.38^\circ$  the peak of axial turbulence is always near the vortex ring core while the radial one is near the impinging plate, where the counter rotating vortex ring should be located. Moreover the shear layer, characterized by high turbulent values, arrives until the impinging plate. At  $\varphi = 73.84^\circ$  the vortex ring is almost out of measurement zone while the high turbulent values are located along the shear layer. It has to be point out that from  $\varphi = 55.38^\circ$  to  $\varphi = 92.30^\circ$  the high turbulent values of the shear layer arrive on the impinging plate and the two shear layers merge on the jet axis far from the orifice plate. Such a triangular region is characterized by zero axial turbulence and very low radial one. For  $\varphi > 92.30^\circ$  these values decrease. In Figure 8 the axial and radial velocity maps, for  $Sr$  equal to 0.044 at  $H/D_0$  equal to 6, are shown. At  $\varphi = 0^\circ$  the ZNMF jet starts coming out and at  $\varphi = 18.46^\circ$  the vortex ring is still forming. From  $\varphi = 36.92^\circ$  to  $\varphi = 129.22^\circ$  the vortex ring convects downstream. During this period of the cycle the maximum of the axial velocity can be detected in the vortex ring centre differently from the lowest Strouhal number case (figure 6) where the maximum is located in the trailing jet (according

to McGuinn et al., 2013). At  $\varphi = 92.30^\circ$  the axial velocity values is slightly decreasing. Then, at  $\varphi = 110.76^\circ$ , when the ZNMF jet begins to approach the impinging plate, the axial values are definitely decreasing. At  $\varphi = 129.22^\circ$  high values of the radial component can be detected near the wall at a radial position where the vortex ring is placed. Then (at  $\varphi = 147.68^\circ$ ), when the axial velocity is still decreasing, the high radial velocity region is still moving with the sweeping vortex ring. The next phase is not reported because no relevant features are present in the field (because the ejection cycle is almost finished). In Figure 9 the mean squared axial and radial turbulent velocity maps, for  $Sr$  equal to 0.044 at  $H/D_0$  equal to 6, are shown. During the formation and convection of the vortex ring ( $0^\circ \leq \varphi \leq 110.76^\circ$ ) the high values of the turbulence are located near the vortex ring and along the shear layer. Furthermore, as in the previous case, high values of axial turbulence can be observed on the front boundary of the vortex ring but not in its centre, differently from the radial one. In this configuration, the triangular region characterized by zero axial turbulence and very low radial turbulence has an extension, in the axial direction, lower than the previous case. At  $\varphi = 110.76^\circ$  the ZNMF jet is going to impinge and the region of high turbulent values increases for both component. Then (at  $\varphi = 129.22^\circ$ ) the high value of axial turbulence is still located near the vortex ring while the radial one shows high values near the vortex ring and also in the region, near the impinging plate, where the interaction between the impinging jet and the plate occurs. In this phase the shear layer, with its high turbulent values, has not arrived near the impinging plate yet and the ZNMF jet is already decelerating. Moreover it is possible to see that near the orifice plate, along the orifice edge, the turbulent values are decreasing. At  $\varphi = 147.68^\circ$  the high turbulent values are still detected moving with the sweeping vortex ring while the shear layer, that has just touched the impinging plate, shows decreasing values. As previously said, even in this case the turbulent velocity values are higher than the case at  $Sr$  equal to 0.011 but similar to those at  $Sr$  equal to 0.022. In Figure 10 the vortex ring trajectory (in the last diameter upstream the impinging plate) for the three different Strouhal numbers at any orifice-to-plate distances are shown. The location of the vortex ring centre has been detected by using the maximum value attains by the Q-criterion (as defined in Jeong and Hussain, 1995) applied to the velocity maps for each phase. At  $H/D_0$  equal to 2 it is possible to highlight that the trajectories show the same path until  $x/D_0$  equal to 1.2. Then a double rebound near the impinging plate is observed. For  $x/D_0 > 1.2$  the vortex ring path of the highest Strouhal number shows the closest position to the plate. The same behaviour can be observed at  $H/D_0$  equal to 4. The unique difference is that the double rebound occurs at higher radial position and is less evident as the Strouhal number decreases. At  $H/D_0$  equal to 6 the curves have a similar behaviour but the second rebound is disappeared. In Figure 11 the saddle point behaviour for the three different Strouhal number values at  $H/D_0$  equal to 2 (for  $\varphi = 295^\circ$ ) is shown. It is where nothing that the distance of the saddle point from the orifice exit increases as the Strouhal number decreases. This is related to the half piston stroke because the higher is  $l_p$  (lower is the Strouhal number) the higher is the volume of fluid injected in and drawn from the ambient. Hence, during the suction phase the saddle point moves towards higher axial position to let the higher requested volume to enter inside the piston-cavity. Such a behaviour is more evident

in this configuration because the ambient is constrained by two plate (the impinging and the orifice ones) so the fluid can not be drawn from the upstream space (as occurs in a nozzle configuration).

## CONCLUSIONS

A fundamental study on the influence of the Strouhal number and the orifice-to-plate distance on the impinging ZNMF jet flow field at high Reynolds number has been carried out. The axial velocity morphology shows a different profile approaching the impinging plate as the orifice-to-plate distance increases. Indeed a bell-shape profile is visible at higher distance while a minimum on the jet axis is detected at the shortest configuration. Furthermore the position along the jet axis of the maximum axial velocity is influenced by the Strouhal number (according to McGuinn et al., 2013). The extension of a region, characterized by low turbulence, decreases as the Strouhal number increases. High turbulence is located, above all, in the vortex ring core and along the shear layer. Such a shear layer has an influence on the flow field which is lower, than the vortex ring one, as the Strouhal number increases. Furthermore the turbulent velocity near the vortex core attains high values at high Strouhal number. The vortex ring trajectory shows a double rebound. The second rebound disappears as the orifice-to-plate distance increases. The Strouhal number also influences the vortex ring trajectory which is closer to the plate, at high radial position, for higher Strouhal number. Finally the saddle point is located farther from the plate as the Strouhal number decreases.

## ACKNOWLEDGMENT

This research was supported by Università degli Studi di Napoli Federico II and Compagnia di San Paolo under the "STAR Program 2013".

The support of the ARC of this research through LIEF grants is gratefully acknowledged.

## REFERENCES

- Abramovich, G. N., 1963, "The Theory of Turbulent Jets", The M.I.T. Press, Cambridge, MA.
- Cater, J. E., and Soria, J., 2002, "The evolution of round zero-net-mass-flux jets", *Journal of Fluid Mechanics*, Vol. 472, pp. 167-200.
- Greco, C. S., Ianiro, A., Astarita, T., and Cardone, G., 2013, "On the near field of single and twin circular synthetic air jets", *International Journal of Heat and Fluid Flow*, Vol. 44, pp. 41-55.
- Greco, C. S., Ianiro, A., and Cardone, G., 2014, "Time and phase average heat transfer in single and twin circular synthetic impinging air jets", *International Journal of Heat and Mass Transfer*, Vol. 73, pp. 776-788.
- Hadžiabdić, M., and Hanjalić, K., 2008, "Vortical structures and heat transfer in a round impinging jet", *Journal of Fluid Mechanics*, Vol. 596, pp. 221-260.
- Holman, R., Utturkar, Y., Mittal, R., Smith, B.L., and Cattafesta, L., 2005, "Formation criterion for synthetic jets", *AIAA Journal*, Vol. 43(10), pp. 2110-2116.
- Hussain, A. K. M. F., and Reynolds, W. C., 1970, "The mechanics of an organized wave in turbulent shear flow", *Journal of Fluid Mechanics*, Vol. 41(02), pp. 241-258.

Jeong, J., and Hussain, F., 1995, "On the identification of a vortex", *Journal of Fluid Mechanics*, Vol. 285, pp. 69-94.

McGuinn, A., Farrelly, R., Persoons, T., and Murray, D.B., 2013, "Flow regime characterization of an impinging axisymmetric synthetic jet", *Experimental Thermal and Fluid Science*, Vol. 47, pp. 241-251.

Pavlova, A., and Amitay, M., 2006, "Electronic cooling using synthetic jet impingement", *Journal of heat transfer*, Vol. 128(9), pp. 897-907.

Shuster, J. M., Smith, D. R., 2007, "Experimental study of the formation and scaling of a round synthetic jet", *Physics of Fluids*, Vol. 19(4), 045109.

Smith, B. L., and Glezer, A., 1998, "The formation and evolution of synthetic jets", *Physics of Fluids*, Vol. 10(9), pp. 2281-2297.

Soria, J., 1996, "An investigation of the near wake of a circular cylinder using a videobased digital cross-correlation particle image velocimetry technique", *Experimental Thermal and Fluid Science*, Vol. 12(2), pp. 221-233.

Soria, J., 1998, "Multigrid approach to cross-correlation digital PIV and HPIV analysis", *Proceedings, 13th Australasian Fluid Mechanics Conference*, Monash University, Melbourne, Australia.

Valiorgue, P., Persoons, T., McGuinn, A., and Murray, D. B., 2009, "Heat transfer mechanisms in an impinging synthetic jet for small jet-to-surface spacing", *Experimental Thermal and Fluid Science*, Vol. 33, pp. 597-603.

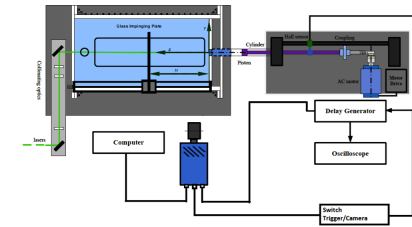


Figure 1. Experimental setup.

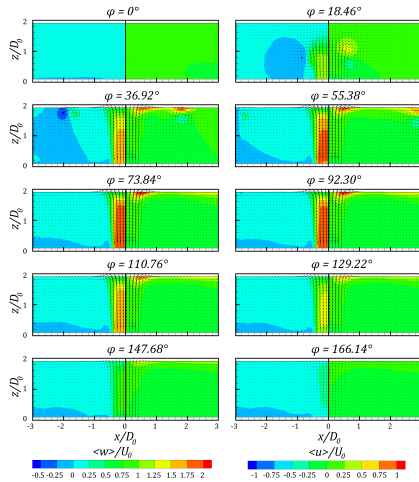


Figure 2. Axial (left) and radial (right) velocity maps at  $H/D_0$  equal to 2 for  $Sr = 0.011$ .

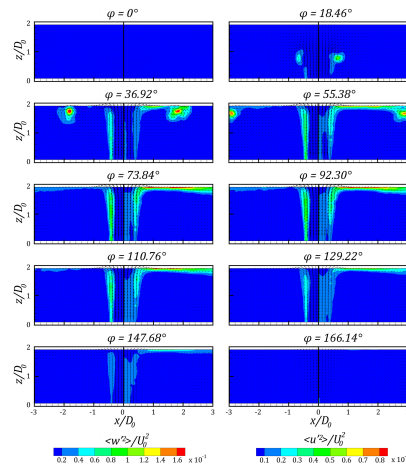


Figure 3. Mean squared axial (left) and radial (right) turbulent velocity maps at  $H/D_0$  equal to 2 for  $Sr = 0.011$ .

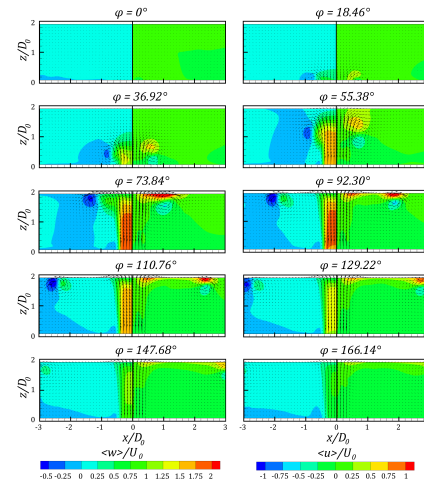


Figure 4. Axial (left) and radial (right) velocity maps at  $H/D_0$  equal to 2 for  $Sr = 0.044$ .

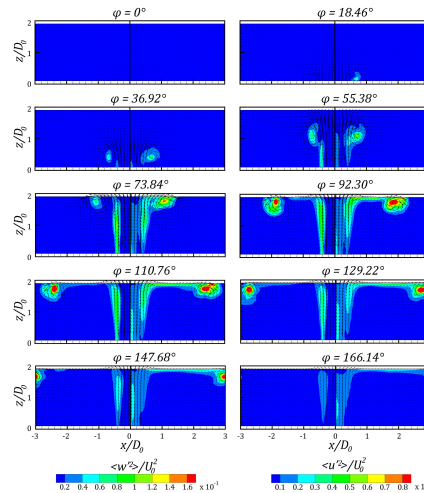


Figure 5. Mean squared axial (left) and radial (right) turbulent velocity maps at  $H/D_0$  equal to 2 for  $Sr = 0.044$ .

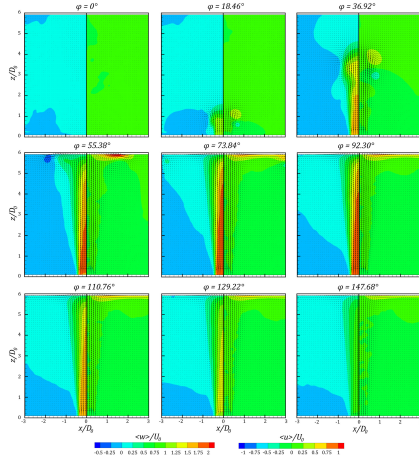


Figure 6. Axial (left) and radial (right) velocity maps at  $H/D_0$  equal to 6 for  $Sr = 0.011$ .

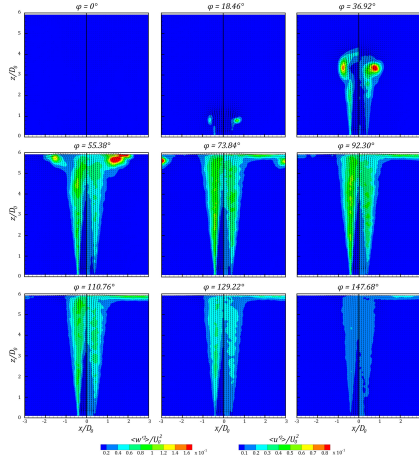


Figure 7. Mean squared axial (left) and radial (right) turbulent velocity maps at  $H/D_0$  equal to 6 for  $Sr = 0.011$ .

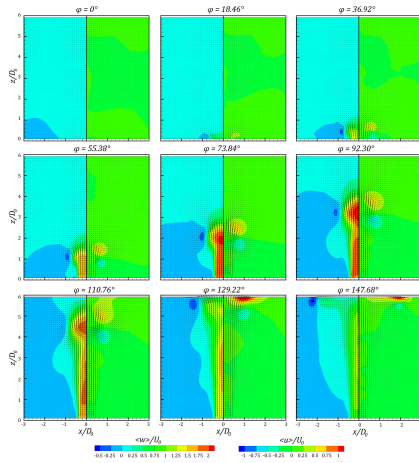


Figure 8. Axial (left) and radial (right) velocity maps at  $H/D_0$  equal to 6 for  $Sr = 0.044$ .

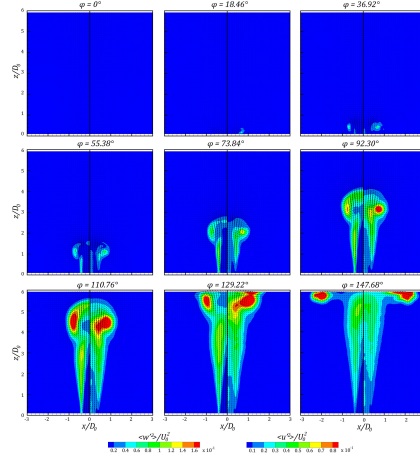


Figure 9. Mean squared axial (left) and radial (right) turbulent velocity maps at  $H/D_0$  equal to 6 for  $Sr = 0.044$ .

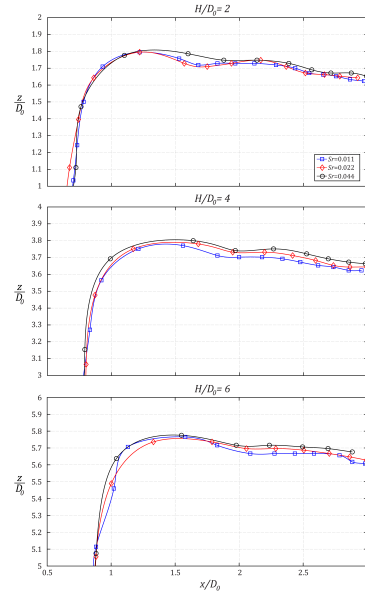


Figure 10. Vortex ring trajectory for all the configurations.

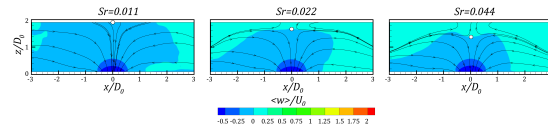


Figure 11. Saddle point location (white spot) for each value of  $St$  at  $H/D_0$  equal to 2 for  $\phi = 295^\circ$ .